SCIENTIFIC REPORTS

OPEN

Unusual properties and potential applications of strain BN-MS_2 (M = Mo, W) heterostructures

Received: 24 October 2018
Accepted: 4 February 2019
Published online: 05 March 2019

Jie Su, Jian He, Junjing Zhang, Zhenhua Lin, Jingjing Chang, Jincheng Zhang & Yue Hao

Heterostructures receive intensive attentions due to their excellent intrinsic properties and wide applications. Here, we investigate the natural physical properties and performances of strain BN-MS_2 (M = Mo, W) heterostructure by density functional theory. Different to compressive monolayer MS_2, corresponding BN-MS_2 heterostructures keep direct band-gap characters because effects of charge transfer on anti-bonding dz^2 orbitals are stronger than those of Poisson effect. Mexican-hat-like bands without magnetic moments are observed at strain BN-MS_2 heterostructures when the compression is enough. Consequently, electron mobilities of strain BN-MS_2 heterostructures are slightly reduced at first and then enlarged with increasing compressive strain. Note that, strain BN-MS_2 heterostructures reduce the band edges of MS_2 layers and extend their application in photocatalytic water splitting. But just the n-type and p-type Schottky barriers of devices with strain BN-MS_2 heterostructures are reduced and even vanished with the increasing tensile and compressive, respectively. Besides, electron mobilities of strain BN-MoS_2 and BN-WS_2 heterostructures can be enhanced to 1290 and 1926 $cm^2 V^{-1} s^{-1}$, respectively, with increasing tensile strain. Interestingly, the exciton binding energies of strain BN-MS_2 heterostructures exhibit oscillation variations, different to those of strain monolayer MS_2.

Two-dimensional transition metal dichalcogenides (TMDs) are an emerging class of materials with atomic thickness, pristine surface, unique and tunable electronic properties which make them highly attractive for applications ranging from nanoelectronics to optoelectronics with high performances[1,2]. However, many studies have revealed that the performances of nanodevices based on TMDs in experiment are lower than the theoretical expectations[1–4]. For examples, most measured carrier mobilities of monolayer MoS_2 nanodevices under room temperature are far lower than the theoretical predication of 410 $cm^2 V^{-1} s^{-1}$ [5–7]. That can be ascribed to three main reasons: first, the fabricated TMDs flakes in experiment containing several defects, like vacancies, which enhance the scattering effects and deteriorate the intrinsic properties of TMDs[8,9]. Second, oxide substrates with surface roughness induce strong interfacial charged impurities at substrates-TMDs interfaces[10–14]. Third, metal-TMDs interfaces usually have large contact resistances and Schottky barrier heights (SBHs) which limit the carrier injection efficiency[15–19]. To overcome these issues, van der Waals heterostructures engineering, especially BN-TMDs heterostructures, have been employed. Moreover, such approaches have evidently improved the performances of nanodevices based on TMDs. For examples, Wang, *et al*. have fabricated MoS_2, $MoSe_2$ and WS_2 layers on hexagonal boron nitride (BN) substrates to form BN-TMDs heterostructures, which enhanced the photoluminescence and room-temperature mobilities of TMDs due to the reduced substrate traps and improved fake quality[20–24]. Liao *et al*. have found that forming BN-TMDs heterostructures in metal-TMDs interface regions not only modulated the work function and fermi level pinning effect, but also reduced the SBHs and contacts resistances of metal-TMDs interfaces by an order of magnitude[25,26]. Moreover, BN-TMDs heterostructures between gate and channel layer could change the main noise source in channel from charged impurities to trapping-detrapping process[27]. Thus, BN-TMDs heterostructures have been widely used in the high performance nanodevices, including integration[28], photoresponse[29], self-biased diode[30], etc.

It should be noted that MS_2 (M = Mo, W) as typical members of TMDs are not only suitable for above mentioned nanodevices, but also have great potentials in applications of flexible nanodevices, such as flexible battery[31],

China State Key Discipline Laboratory of Wide Band Gap Semiconductor Tecchnology, Shaanxi Joint Key Laboratory of Graphene, Advanced Interdisciplinary Research Center for Flexible Electronics, School of Microelectronics, Xidian University, Xi'an, 710071, China. Correspondence and requests for materials should be addressed to J.C. (email: jjingchang@xidian.edu.cn)

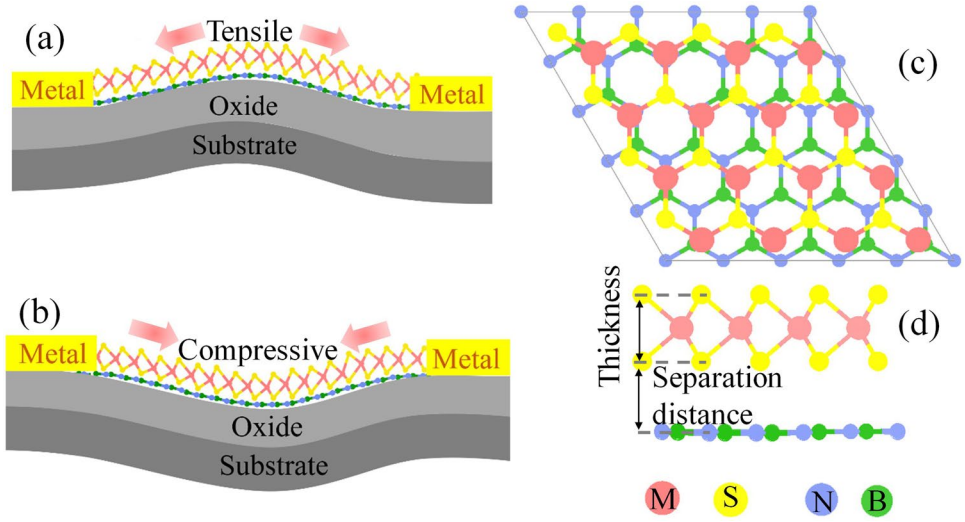

Figure 1. Schematics of BN-MS_2 heterostructures nanodevices with (**a**) tensile and (**b**) compressive strain. (**c**) Top and (**d**) side views of BN-MoS_2 heterostructures.

	Without strain			4% tension	4% compression
	Lattice constant (Å)	Band gap (eV)	Thickness (Å)	Thickness (Å)	Thickness (Å)
Monolayer BN	2.51, 2.49[43], 2.50[45]	4.57, 4.82[45]	—	—	—
Monolayer MoS_2	3.168, 3.16[47], 3.18[48]	1.76, 1.74[47], 1.67[48]	3.12	3.05	3.23
Monolayer WS_2	3.153, 3.146[44], 3.152[46]	1.91, 1.94[49], 1.82[48]	3.15	3.07	3.25
BN-MoS_2 heterostructure	12.672	1.72	3.13	3.05	3.22
BN-WS_2 heterostructure	12.612	1.88	3.14	3.06	3.24

Table 1. Lattice constants and band gaps of strain monolayer BN, MS_2, and BN-MS_2 heterostructures (M = W, Mo). The thicknesses of isolated MS_2 layers and MS_2 layers in the heterostructures are also listed for comparison.

humidity sensing[32], flexible supercapacitor[33], and so on. However, the performances of flexible nanodevices based on MS_2, like carrier mobilities, in experiment are far lower than expectation[34–36]. Moreover, direct-to-indirect transitions occur in band gaps of monolayer MS_2 in the flexible nanodevices[37–41]. Such characters are not conductive to realize high performance flexible nanodevices. Inspired by the excellent performance of BN-TMDs heterostructure in optoelectronics as above mentioned, forming strain BN-MS_2 heterostructure with great potential to improve the performance flexible nanodevices. However, few studies have focused on the strain BN-MS_2 heterostructures, although the carrier mobilities of monolayer MoS_2 flexible transistors had been enlarged from 30 to 45 $cm^2 V^{-1} s^{-1}$ when monolayer MoS_2 was substituted by strain BN-MoS_2 heterostructure[34,42]. Moreover, so far few theoretical studies have focused on the natural physical properties of strain BN-MS_2 heterostructures. Hence, in this work, the electronic, magnetic, transport, optical properties, and additional potential application of strain BN-MS_2 (M = Mo, W) heterostructures were comprehensively investigated by first principles calculations.

Results and Discussion

Geometric structure. Before exploring the strain BN-MS_2 (M = Mo, W) heterostructures (Fig. 1a,b), the geometric structures of isolated monolayer BN, MoS_2, WS_2 were investigated and listed in Table 1. The lattice constants of isolated monolayer BN and MS_2 are in good agreement with previous studies[43–48]. BN-MS_2 heterostructures are constructed by stacking the BN and MS_2 monolayers on top of each other. To study the natural physical properties of strain BN-MS_2 heterostructures accurately, 5×5 BN supercells are constructed and strained to match with the 4×4 MS_2 supercells, as shown in Fig. 1. The lattice mismatches of BN-MoS_2 and BN-WS_2 heterostructures are less than 1%. The equilibrium separations of BN-MoS_2 and BN-WS_2 heterostructures are 3.28 Å and 3.15 Å, respectively, after extensive test.

Electronic properties. To well understand the electronic properties of strain BN-MS_2 heterostructures, the electronic structures of corresponding isolated strain monolayer MS_2 are studied firstly. Figure 2a as an example

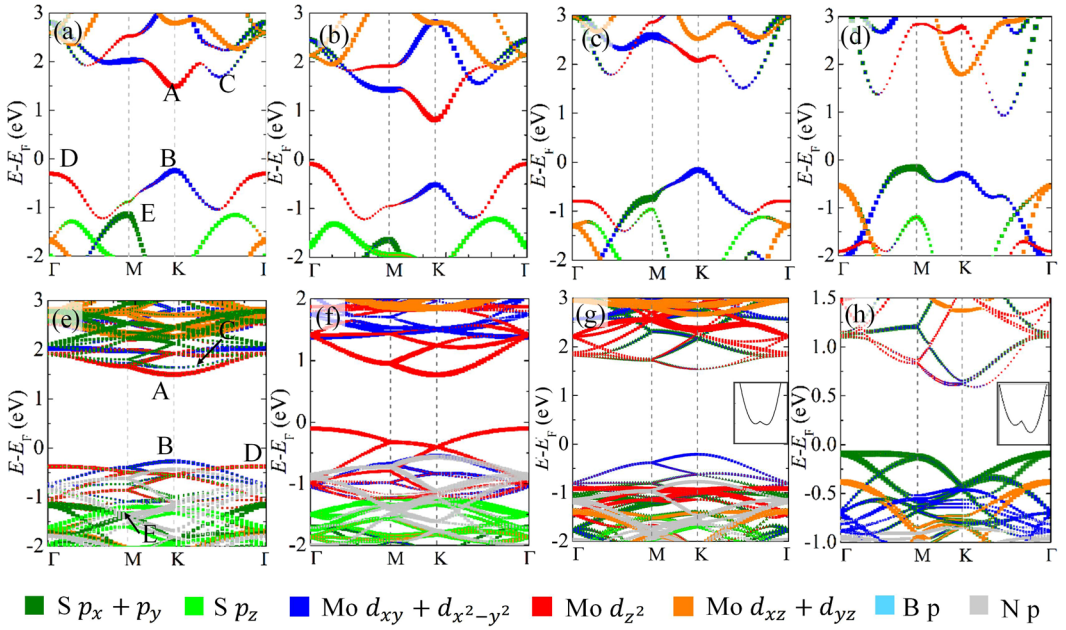

Figure 2. Projected band structures of monolayer MoS_2 (**a**) without strain, and with (**b**) 4% tensile, (**c**) 4% compressive and (**d**) 10% compressive strains, respectively. Projected band structures of BN-MoS_2 heterostructures (**e**) without strain, and with (**f**) 4% tensile, (**g**) 4% compressive and (**h**) 12% compressive strains, respectively. The insertions in (**g**) and (**h**) are the conduction bands around the K points.

displays the electronic structure of monolayer MoS_2. Monolayer MoS_2 is a direct band gap semiconductor with conduction band minimum (CBM) (*viz.* band A) and valence band maximum (VBM) (*viz.* band B) at K point. Moreover, its CBM and VBM are mainly dominated by anti-bonding d_{z^2} and bonding $d_{x^2-y^2} + d_{xy}$ orbitals of Mo atoms, respectively. Such characters are consistent with previous reports[41]. In addition, other special bands C, D, and E (marked in Fig. 2a) of monolayer MoS_2 are mainly composed of anti-bonding $d_{x^2-y^2} + d_{xy}$ orbitals, bonding d_{z^2} orbitals of Mo atoms, and bonding $p_x + p_y$ orbitals of S atoms, respectively, as demonstrated in Fig. 2a. Similar characters, except for the band gap, are also observed in monolayer WS_2, as shown in Fig. S1. The direct band gaps of monolayer MoS_2 and WS_2 are 1.76 and 1.91 eV, respectively, which are in accordance with previous reports[44–49] and listed in Table 1. Note that, although these band gaps are lower than the experimental values[50], they are closer to the transport band gaps in nanodevices compared to the band gap calculated by GW and HSE functional[19,51]. That is because the strong Coulombic screening by metal electrodes can minimize the exciton binding energies and many body effects of 2D materials[16,27]. Moreover, the electronic structures of MS_2 calculated by PBE functional are similar to those calculated by HSE functional (as demonstrated in Fig. S2). It suggests that PBE functional is sufficient to study the electronic properties of MS_2 layers and BN-MS_2 heterostructures.

When monolayer MS_2 undergoes tensile strain, the band gap reduces gradually and accompanies with a direct-to-indirect band gap transition. That is because the thickness of MS_2 (as listed in Table 1) is reduced by tensile strains due to the Poisson effect. Such thickness reduction strengthens the coupling between the p_z orbitals of S atoms and d_{z^2} orbitals of M atoms, and such biaxial tensile strain weakens the coupling between the $p_x + p_y$ orbitals of S atoms and $d_{x^2-y^2} + d_{xy}$ orbitals of M atoms. As a result, the energies of anti-bonding band A and bonding band B reduce, and the energies of anti-bonding band C and bonding band D enlarge. Thus, the VBM shifts up and moves from K to Γ point, and the CBM at the K point shifts down, leading to the reduction of band gaps with increasing tensile strain, as shown in Fig. 2b. On the contrary, application of compressive strain enlarges the thickness of monolayer MS_2 (as listed in Table 1), and then weakens the coupling between the p_z orbitals of S atoms and d_{z^2} orbitals of M atoms and enhances coupling between the $p_x + p_y$ orbitals of S atoms and $d_{x^2-y^2} + d_{xy}$ orbitals of M atoms. Consequently, the anti-bonding bands A and C shift up and down, respectively. The position of CBM transforms from anti-bonding band A to anti-bonding band C, leading to a direct-to-indirect band gap transition, as displayed in Fig. 2c,d. Nevertheless, it should be noted that the energy of anti-bonding band C is higher than that of anti-bonding band A of monolayer MS_2 without strain, and it decreases slightly with the increasing compressive strain. As a result, the energy of band C of monolayer MS_2 with small compressive strain is still higher than that of band A of monolayer MS_2 without strain. Thus, the band gaps of monolayer MS_2 slightly enlarge at first and then decrease with the increasing enlarge compressive strain, as displayed in Fig. 3a, which is consistent with previous reports[41]. In addition, the enhanced coupling between the $p_x + p_y$ orbitals of S atoms and $d_{x^2-y^2} + d_{xy}$ orbitals of M atoms induced by compressive strain also rises the energy of bonding band E, as shown in Fig. 2c. When the compressive strain is larger than 8%, such raised bonding band E can surpass that of raised bonding band B. Consequently, the position of VBM shifts from the bonding band B at the K point to bonding band E at the M point, leading to a direct-to-indirect transition, as shown in Fig. 2d.

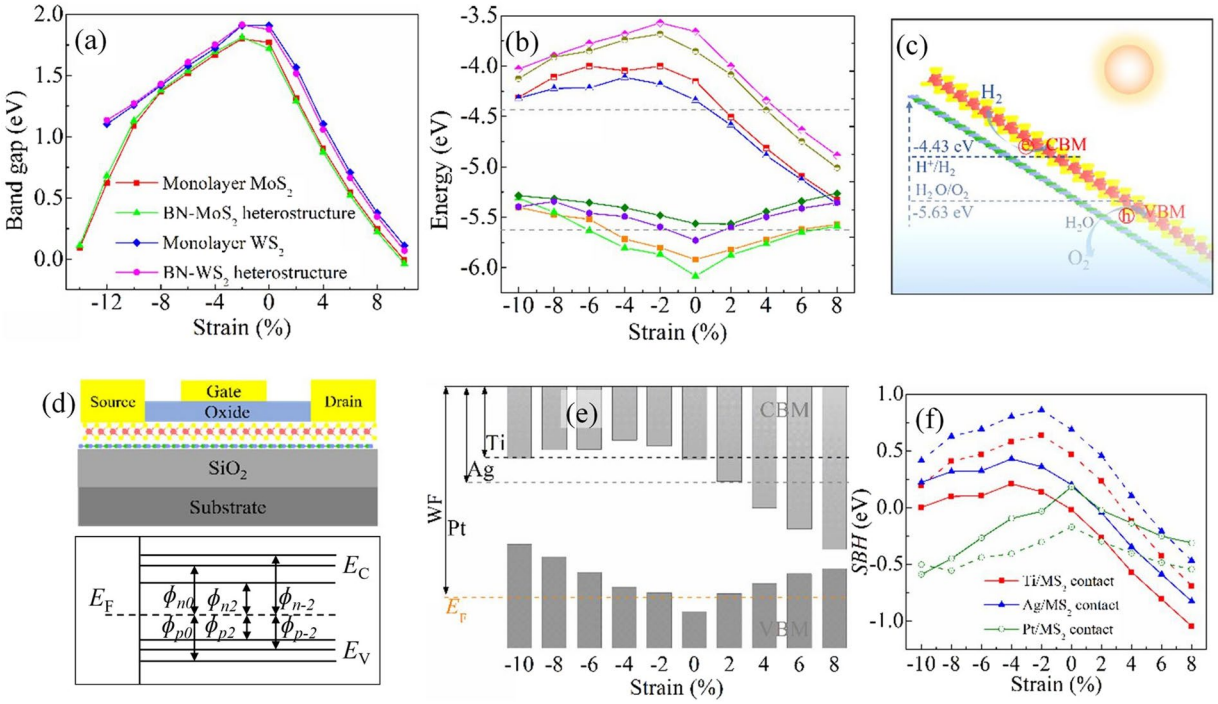

Figure 3. (**a**) Band gaps and (**b**) band edges of monolayer MS_2 and BN-MS_2 heterostructures as functions of strain, respectively. The square, triangle, rhombus, and circle indicate the monolayer MoS_2, BN-MoS_2 heterostructure, monolayer WS_2, and BN-WS_2 heterostructure, respectively. The up and low gray dash lines in Figure (**b**) represent the water reduction and oxidation potential levels, respectively. (**c**) Schematic illustration for BN-MS_2 heterostructure used in the photocatalysis for water splitting. (**d**) Sketch of SBHs at metal/MS_2 interfaces in transistors based on BN-MS_2 heterostructure. (**e**) Band diagrams of metal Ti, Ag, Pt, and strain BN-MoS_2 heterostructures. WF and E_F denote the work function and Fermi level of metal, respectively. (**f**) The ideal n-type SBHs of Ti/MS_2 and Ag/MS_2 contacts and p-type SBHs of Pt/MS_2 contacts as functions of the strain BN-MS_2 heterostructures. The solid and dash lines represent the metal/MoS_2 and metal/WS_2 interfaces, respectively.

For BN-MS_2 heterostructures, their CBM and VBM are dominated by the MS_2 layer, such as the BN-MoS_2 heterostructure in Fig. 2e. Moreover, the components and positions of CBM and VBM of BN-MS_2 heterostructures are similar to those of monolayer MS_2. It suggests that the intrinsic electronic properties can be remained when monolayer MS_2 transforms to type-I BN-MS_2 heterostructure. However, the band gaps reduce slightly to be 1.72 and 1.88 eV for BN-MoS_2 and BN-WS_2 heterostructures, respectively. That is because the weak charge transfer between BN and MS_2 layers (as shown in Fig. S3) slightly reduce the anti-bonding band A. When BN-MS_2 heterostructures undergo tensile strain, they keep type-I heterostructure characters, and their CBM and VBM are still dominated by MS_2 layer. Moreover, variations of band gaps and band edges of tensile BN-MS_2 heterostructures (see Fig. 2f) are similar to those of tensile monolayer MS_2 since the biaxial tensile also induces the reduction of MS_2 layer thickness in BN-MS_2 heterostructures (as listed in Table 1). However, the reduction indirect band gaps of tensile BN-MS_2 heterostructures are slightly lower than those of corresponding tensile monolayer MS_2, as exhibited in Fig. 3a. That is because additional charges are accumulated at the MS_2 layer of BN-MS_2 heterostructures (as displayed in Fig. S3), which can further reduce the energy of anti-bonding d_{z^2} (*viz.* band A). In the case of BN-MS_2 heterostructures with compressive strain, they keep type-I heterostructure characters. The MS_2 layer of compressive BN-MS_2 heterostructures are still direct band semiconductor with CBM and VBM located at K point, as displayed in Fig. 2g. This is different to those of corresponding monolayer MS_2 although compressive strain also induces the enlarged thickness of MS_2 layer. That is because although the Poisson effect rises the anti-bonding orbitals d_{z^2} and reduces the anti-bonding orbitals $d_{x^2-y^2} + d_{xy}$, the charge transfer between BN and MS_2 layers reduces the anti-bonding orbitals d_{z^2} and $d_{x^2-y^2} + d_{xy}$. Hence, the energy of anti-bonding band C is still higher than that of anti-bonding band A at the K point which dominates the CBM of BN-MS_2 heterostructure. It should be noted that, except for the Poisson effect induced by compressive strain, the wrinkle phenomenon is also introduced to the MS_2 layer of BN-MS_2 heterostructure as the compressive strain continue to increases, which induce a heterogeneous charge transfer between BN and MS_2 layers of BN-MS_2 heterostructures (as displayed in Fig. S4). As a result, the energy of anti-bonding orbitals $d_{x^2-y^2} + d_{xy}$ is close to that of anti-bonding orbitals d_{z^2}, and a Mexican-hat-like band around K point is formed, as shown in Fig. 2g,h. In general, the Mexican-hat-bands suggesting an obviously magnetic moments[52]. Nevertheless, nonmagnetic states are observed for BN-TMDs with larger compressive strain, as displayed in Fig. S5. When the compressive strain continues enlarging, such a Mexican-hat-like band becomes more evident, and a direct-to-indirect band gap transition is

observed, as displayed in Fig. 2h. That is because the weak interaction is insufficient to hamper the increasing energy of the bonding band E at the M point.

Band levels and applications. Figure 3b displays the band edges of BN-MS_2 heterostructures and monolayer MS_2 on an absolute energy scale with respect to the vacuum level. For monolayer MS_2, their band edges of VBM and CBM states of monolayer MoS_2 and WS_2 are −5.97, −4.18 eV and, −5.56, −3.63 eV, respectively, which are consistent with previous reports[49]. The VBMs are enhanced with both the increasing compressive and tensile strains since compressive and tensile strain can enhance the bonding band B and bonding band D, respectively. The CBMs reduce monotonously with the increasing tensile strain, while they enlarge at first and then reduce with the increasing compressive strain due to the transfer of CBM due to the transformation of CBM, as above analysis. For strain BN-MS_2 heterostructures, similar characters are observed. Nevertheless, the band edges of BN-MS_2 heterostructures are lower than those of corresponding MS_2 due to the charge transfer between BN and MS_2 layer, as above analysis.

It is well known that the band levels are related to the applications in photocatalytic and electronic fields. Figure 3c demonstrates the schematic of photocatalytic water splitting. A good photocatalytic material for water-splitting requires that the CBM and VBM are lower and higher than the reduction and oxidation potentials of water, respectively[49]. Thus, monolayer WS_2 is not a good photocatalytic material, as displayed in Fig. 3b. However, the CBM and VBM of BN-WS_2 heterostructures are higher and lower than reduction and oxidation potentials of water, respectively. Moreover, such characteristics remain when the compressive and tensile strains of BN-WS_2 heterostructures are lower than 2%. In other words, forming BN-WS_2 heterostructures can extend the application of monolayer WS_2 in the photocatalytic water splitting. For the monolayer MoS_2, its band edges are outside of the reduction and oxidation potentials of water when compressive strain is lower than 4%. It means that monolayer MoS_2 may be suitable for the application of photocatalytic water splitting, but the compressive strain is limited to be 4%. Upon forming BN-MoS_2 heterostructure, similar characters can be observed when the compressive strain is up to 6%. It suggests that forming BN-MoS_2 heterostructures can extend the application of strain monolayer MoS_2 in photocatalytic water splitting.

Figure 3d displays the schematic diagrams of metal/semiconductor contacts in FETs which is usually used to calculate ideal SBH values according to Schottky-Mott rule without Fermi level pinning. For metal/MS_2 contacts with strong Fermi level pinning effects, their large SBHs are difficult to be obtained by such methods, and they are difficult to be reduced and vanished by strained monolayer MS_2. Different to metal/MS_2 contacts, metal/MoS_2 contacts with BN-MoS_2 heterostructures show negligible Fermi level pinning effect[16,18]. The SBHs at metal/MoS_2 contacts with strain BN-MS_2 heterostructures can be obtained directly from the difference between band levels heterostructures and work functions (WFs) of metal electrodes. Figure 3e as an example shows the relationship between the WFs of metal and strain BN-MoS_2 heterostructure. No matter what the work function of metal electrode, the n-type and p-type SBHs reduce with the increasing tensile and compressive strain of BN-MoS_2 heterostructures, respectively. The detailed variations of SBHs of metal/MoS_2 contacts induced by strained BN-MoS_2 heterostructures as displayed in Fig. 3f. The ideal n-type SBHs of Ti/MoS_2, and Ag/MoS_2 contacts with BN-MoS_2 heterostructures are −0.02 and 0.20 eV, respectively, which are lower than those of pure metal/MoS_2 contacts[16,18]. When BN-MoS_2 heterostructures undergo tensile strain, these n-type SBHs continue reducing and even vanishing, as exhibited in Fig. 3f. For examples, the lowest n-type SBHs of Ti/MoS_2, and Ag/MoS_2 contacts with tensile BN-MoS_2 heterostructures are low to −1.04 and −0.83 eV, respectively. In addition, the p-type SBH of Pt/MoS_2 contact with BN-MoS_2 heterostructure is about 0.19 eV which is far lower than that of pure Pt/MoS_2 contact[16,18]. Moreover, such p-type SBH can be further vanished when the compressive strain is larger than 2%, as shown in Fig. 3f. As to metal/WS_2 contacts with strain BN-WS_2 heterostructures, similar characteristics are also found, as displayed in Fig. 3f. Such results indicate that substituting strain monolayer MS_2 in flexible devices by strain BN-MS_2 heterostructures can realize high performance MS_2 devices with low contact properties.

Transport properties. Figure 4 gives the carrier effective masses and room-temperature mobilities of strained monolayer MS_2 and BN-MS_2 heterostructures. For monolayer MS_2, the electron and hole mobilities at room-temperature of monolayer MoS_2 and WS_2 are 77.17, 155.79 $cm^2 V^{-1} s^{-1}$, and 163.22, 651.56 $cm^2 V^{-1} s^{-1}$, respectively, and the effective electron and hole masses of monolayer MoS_2 and WS_2 are 0.48, 0.64 m_0, and 0.30, 0.38 m_0, respectively, which are in good agreement with previous reports[48,53]. These effective electron masses reduce because either compressive or tensile strains are added to monolayer MS_2. These effective hole masses enhance at first and then reduce with the increasing tensile strain since the position of VBM occurs a K-to-Γ transition; while they enlarge monotonically with the increasing compressive strain. Note that, when the compressive strain is larger than 8%, partial effective hole masses are reduced significantly, indicating an evidently anisotropic transport properties for monolayer MS_2 with large compressive strain. That is because a K-to-M transition occurs at the position of VBM when the compressive strain is larger than 8%. In general, the small effective mass indicates the large carrier mobility. As a result, the variations of electron and hole mobilities of strain monolayer MS_2 are opposite to these of corresponding effective masses, as exhibited in Fig. 4. In other words, both compressive and tensile strains can enlarge the electron mobilities of monolayer MS_2. It should be noted that, nevertheless, the experimental electron mobilities of strain monolayer MS_2 in flexible nanodevices are lower than those of monolayer MS_2 due to the interfacial charged impurities induced by Si/SiO_2 substrates with large surface roughness[4,34].

For BN-MS_2 heterostructures, the effective electron and hole masses of BN-MoS_2 and BN-WS_2 heterostructures are 0.47, 0.57 m_0, and 0.28, 0.37 m_0, respectively, which are slightly lower than those corresponding values of monolayer MS_2. It means higher carrier mobilities for BN-MS_2 heterostructures compared to monolayer MS_2. The enhanced electron and hole mobilities of BN-MoS_2 and BN-WS_2 heterostructures are 223.50, 213.20 $cm^2 V^{-1} s^{-1}$, and 505.04, 751.63 $cm^2 V^{-1} s^{-1}$, respectively. When BN-MS_2 heterostructures undergo tensile strain, their effective electron masses are lower than those of corresponding tensile monolayer MS_2. An opposite phenomenon

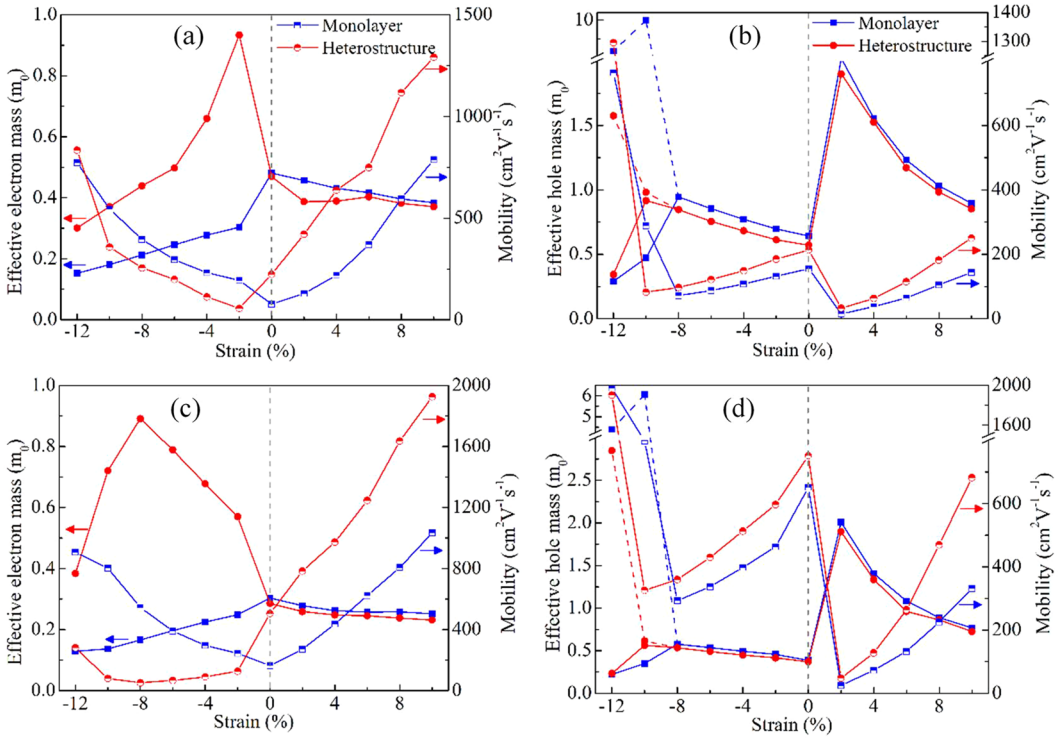

Figure 4. Effective masses and room-temperature mobilities of strain monolayer MS_2 and BN-MS_2 heterostructures: (**a**) electron of MoS_2, (**b**) hole of MoS_2, (**c**) electron of WS_2, (**d**) hole of WS_2.

occurs for BN-MS_2 heterostructures with compressive strain. Moreover, different to monolayer MS_2, the effective electron masses of BN-MS_2 heterostructures reduce monotonically with the increasing tensile strain, while they enlarge at first and then reduce with the increasing compressive strain since the increased compressive strain induces the formation of a Mexican-hat-like band gradually. As a result, the enhanced room-temperature electron mobilities of BN-MS_2 heterostructures can be further enlarged with the increasing tensile strain, and are higher than those of corresponding monolayer MS_2; while they reduce at first and then enlarge with the increasing compressive strain. It should be noted that the lowest electron mobilities of BN-MS_2 heterostructure are close to that of monolayer MS_2, although the electron mobilities of compressive BN-MS_2 heterostructure are lower than those of corresponding compressive MS_2, as shown in Fig. 4a,c. For examples, the lowest electron mobility of BN-MoS_2 heterostructure of about 56.48 $cm^2 V^{-1} s^{-1}$ is close to that of monolayer MS_2 of about 77.16 $cm^2 V^{-1} s^{-1}$. In addition, BN layer without dangling bonds can strongly weaken the interfacial charged scattering. Such characters suggest that flexible nanodevices based on BN-MS_2 heterostructures can obtain higher electron mobilities than MS_2 flexible nanodevices in experiment[42]. For the hole transport properties of BN-MS_2 heterostructures, the variations of effective masses and mobilities are similar to those of monolayer MS_2, except for the lower effective hole masses and higher room-temperature hole mobilities. However, the hole mobilities of BN-MS_2 heterostructures with small tensile strain are lower than those of pure monolayer MS_2. For example, the hole mobility of BN-MoS_2 heterostructure with 2% tensile strain is about 32.72 $cm^2 V^{-1} s^{-1}$ which is far lower than that of pure monolayer MoS_2 of about 155.79 $cm^2 V^{-1} s^{-1}$.

Optical properties. Except for the transport properties, the variations of effective masses can also modulate the exciton binding energies. The calculated exciton binding energies of monolayer MoS_2 and WS_2 are about 0.98 and 0.61 eV, respectively, which are close to previous studies[53–58]. Moreover, these exciton binding energies enlarge at first and then reduce as the strain changes from compressive to tensile. Upon forming the BN-MoS_2 and BN-WS_2 heterostructures, the exciton binding energies are enhanced 1.05 and 0.65 eV, respectively, because MS_2 layers accept charges from BN layers[55], as shown in Fig. S3. Interestingly, the exciton binding energies of strain BN-MS_2 heterostructures exhibit oscillation variation, just like a "M", as demonstrated in Fig. 5a. In addition, the absorption coefficients of strain BN-MS_2 heterostructures are enlarged compared to those monolayer MS_2, no matter what strains are added to monolayer and BN-MS_2 heterostructures, as the examples illustrated in Fig. 5b.

Conclusion

In summary, electronic and optical properties of strain monolayer MS_2 and BN-MS_2 heterostructures and their potential performance are comprehensively investigated by density functional theory. All strain BN-MS_2 heterostructures are type-I heterostructures, irrespective of compressive and tensile strain. However, different to the indirect band gap characters of compressive monolayer MS_2, corresponding compressive BN-MS_2 heterostructures keep direct band gap characters because effects of charge transfer on anti-bonding d_{z2} orbitals are stronger than those of Poisson effect. Moreover, Mexican-hat-like bands without magnetic moments are observed for

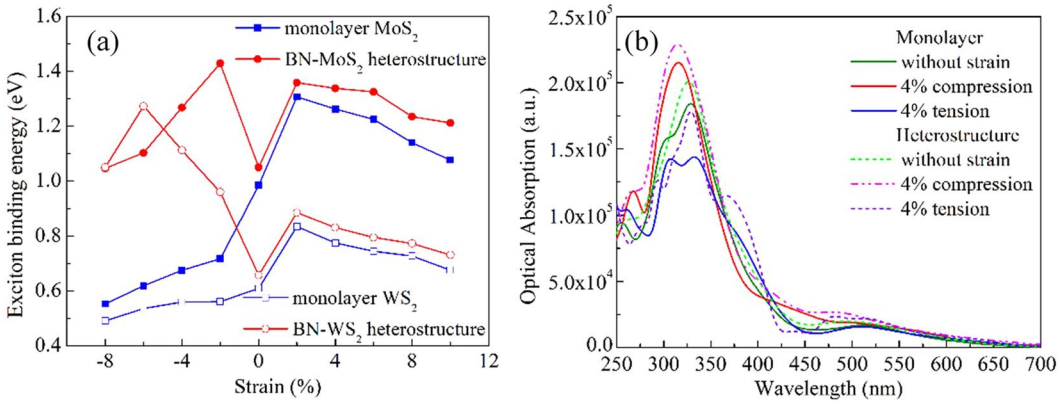

Figure 5. (**a**) Exciton binding energies of monolayer MS_2 and BN-MS_2 heterostructures as functions of strain. (**b**) Optical absorption of monolayer MoS_2 and BN-MoS_2 heterostructures with different strains.

compressive BN-MS_2 heterostructures due to the non-uniform charge transfer induced by wrinkle. Consequently, electron mobilities of flexible devices with BN-MS_2 heterostructures are reduced at first and then enlarged with the increasing compressive strain, different to those of compressive monolayer MS_2. In addition, although strain can induce similar variations of band edges between BN-MS_2 heterostructures and monolayer MS_2, and extend their application in photocatalytic water splitting, strain just can reduce the Schottky barriers of devices with BN-MS_2 heterostructures. Moreover, the n-type and p-type Schottky barriers are reduced and even vanished with the increasing tensile and compressive strain, respectively. For tensile BN-MS_2 heterostructures, variations of their transport properties are similar to those of monolayer MS_2, except for higher electron and hole mobilities and lower effective electron and hole masses. The room-temperature electron mobilities of MoS_2 and WS_2 layers in tensile BN-MS_2 heterostructures can be up to 1290 and 1926 $cm^2 V^{-1} s^{-1}$, respectively. In addition, the exciton binding energies of strain BN-MS_2 heterostructures exhibit oscillation variations, different to those of strain monolayer MS_2.

Computational Methodology

All calculations were performed within first-principles density functional theory (DFT) using projector augmented-wave (PAW) pseudopotentials, as implemented in the Vienna Ab Initio Simulation Package (VASP)[59,60]. The Generalized Gradient Approximaton (GGA) parameterized by Perdew-Burke-Ernzerhof (PBE)[61] was employed to adopt for the exchange-correction functional. The van der Waals (vdW) interactions were considered using the method of Grimme (D2). The cut-off energy was set to be 450 eV. The convergence criterions were 1×10^{-6} eV for the self-consistent field energy and 0.01 eV/Å for the residual forces on each atom, respectively. The Monkhorst-Pack k-point mesh was sampled with a separation of about 0.015 $Å^{-1}$ in the Brillouin zone during the relaxation and electronic calculation periods. To minimize the interlayer interactions under the periodic boundary condition, vacuums of 15 Å were added perpendicular to the layer planes of heterostructure.

The carrier mobilities were calculated by the following expression[62],

$$\mu = \frac{2e\hbar^3 C}{3k_B T |m^*|^2 E^2}$$

where $\hbar$ is the Planck constant, k_B is Boltzmann constant, T is the temperature (set to be 300 K). m^* is the effective mass which is calculated by $m^* = \hbar^2[\partial^2\mathcal{E}(k)/\partial k^2]^{-1}$. E is the deformation potential constant which denotes the shift of the band edges induced by strain. C is the elastic modulus of a uniformly deformed crystal for simulating the lattice distortion activated by the strain, defined by $C = [\partial^2 E/\partial\delta^2]/S_0$, where E is the total energy of the supercell, δ is the applied uniaxial strain, and S_0 is the area of the optimized supercell.

All the exciton binding energies of monolayer MS_2 and BN-MS_2 heterostructures were calculated by adopting the simplified hydrogen-like Wannier-Mott exciton modes[56,57]

$$E_b = \mu_{ex} R_y / m_0 \varepsilon_r^2$$

where E_b is the excition binding energy, μ_{ex} is the reduced exciton mass ($\mu_{ex} = m_e \times m_h/(m_e + m_h)$), m_e and m_h are the effective electron and hole masses, respectively, R_y is the atomic Rydberg energy, and ε_r is the relative dielectric constant.

References

1. Duan, X., Wang, C., Pan, A., Yu, R. & Duan, X. Two-dimensional transition metal dichalcogenides as atomically thin semiconductors: opportunities and challenges. *Chem. Soc. Rev.* **44**, 8859–8876 (2015).
2. Wang, F. *et al.* Progress on electronic and optoelectronic devices of 2D layered semiconducting materials. *Small* **13**, 1604298 (2017).
3. Zhang, W., Huang, Z., Zhang, W. & Li, Y. Two-dimensional semiconductors with possible high room temperature mobility. *Nano Res.* **7**, 1731–1737 (2014).

4. Liu, B., Abbas, A. & Zhou, C. Two-dimensional semiconductors: from materials preparation to electronic applications. *Adv. Electron. Mater.* **3**, 1700045 (2017).
5. Huo, N. *et al*. High carrier mobility in monolayer CVD-grown MoS_2 through phonon suppression. *Nanoscale* **10**, 15071–15077 (2018).
6. Kaasbjerg, K., Thygesen, K. S. & Jacobsen, K. W. Phonon-limited mobility in n-type single-layer MoS_2 from first principles. *Phys. Rev. B* **85**, 115317 (2012).
7. Xie, L. *et al*. Graphene-contacted ultrashort channel monolayer MoS_2 transistors. *Adv. Mater.* **29**, 1702522 (2017).
8. Hong, J. *et al*. Exploring atomic defects in molybdenum disulphide monolayers. *Nat. Commun.* **6**, 6293 (2015).
9. Qiu, H. *et al*. Hopping transport through defect-induced localized states in molybdenum disulphide. *Nat. Commun.* **4**, 2642 (2013).
10. Yu, S. *et al*. Study of interfacial strain at the α-Al_2O_3/monolayer MoS_2 interface by first principle calculations. *Appl. Surf. Sci.* **428**, 593–597 (2018).
11. Chae, W. H., Cain, J. D., Hanson, E. D., Murthy, A. A. & Dravid, V. P. Substrate-induced strain and charge doping in CVD-grown monolayer MoS_2. *Appl. Phys. Lett.* **111**, 143106 (2017).
12. Amani, M. *et al*. Growth-substrate induced performance degradation in chemically synthesized monolayer MoS_2 field effect transistors. *Appl. Phys. Lett.* **104**, 203506 (2014).
13. Yu, Z. *et al*. Analyzing the carrier mobility in transition-metal dichalcogenide MoS_2 field-effect transistors. *Adv. Funct. Mater.* **27**, 1604093 (2017).
14. Lu, X. *et al*. Large-Area Synthesis of monolayer and few-layer $MoSe_2$ films on SiO_2 substrates. *Nano Lett.* **14**, 2419–2425 (2014).
15. Liu, W. *et al*. Role of metal contacts in designing high-performance monolayer n-Type WSe_2 field effect transistors. *Nano Lett.* **13**, 1983–1990 (2013).
16. Gong, C., Colombo, L., Wallace, R. M. & Cho, K. The unusual mechanism of partial fermi level pinning at metal–MoS_2 interfaces. *Nano Lett.* **14**, 1714–1720 (2014).
17. Su, J., Li, N., Zhang, Y., Feng, L. & Liu, Z. Role of vacancies in tuning the electronic properties of Au-MoS_2 contact. *AIP Adv.* **5**, 077182 (2015).
18. Su, J., Feng, L., Zhang, Y. & Liu, Z. The modulation of Schottky barriers of metal–MoS_2 contacts via BN–MoS_2 heterostructures. *Phys. Chem. Chem. Phys.* **18**, 16882–16889 (2016).
19. Wang, Y. *et al*. Does p-type ohmic contact exist in WSe_2–metal interfaces? *Nanoscale* **8**, 1179–1191 (2016).
20. Iqbal, M. W. *et al*. High-mobility and air-stable single-layer WS_2 field-effect transistors sandwiched between chemical vapor deposition-grown hexagonal BN films. *Sci. Rep.* **5**, 10699 (2015).
21. Li, L. *et al*. Raman shift and electrical properties of MoS_2 bilayer on boron nitride substrate. *Nanotechnology* **26**, 295702 (2015).
22. Yan, A. *et al*. Direct growth of single- and few-layer MoS_2 on h-BN with preferred relative rotation angles. *Nano Lett.* **15**, 6324–6331 (2015).
23. Wan, Y. *et al*. Origin of improved optical quality of monolayer molybdenum disulfide grown on hexagonal boron nitride substrate. *Small* **12**, 198–203 (2016).
24. Yu, Y. *et al*. Engineering substrate interactions for high luminescence efficiency of transition-metal dichalcogenide monolayers. *Adv. Funct. Mater.* **26**, 4733–4739 (2016).
25. Wang, J. *et al*. High mobility MoS_2 transistor with low schottky barrier contact by using atomic thick h-BN as a tunneling layer. *Adv. Mater.* **28**, 8302–8308 (2016).
26. Cui, X. *et al*. Low-temperature ohmic contact to monolayer MoS_2 by van der Waals bonded Co/h-BN electrodes. *Nano Lett.* **17**, 4781–4786 (2017).
27. Joo, M.-K. *et al*. Understanding coulomb scattering mechanism in monolayer MoS_2 channel in the presence of h-BN buffer layer. *ACS Appl. Mater. Interfaces* **9**, 5006–5013 (2017).
28. Park, H., Shin, G. H., Lee, K. J. & Choi, S.-Y. Atomic-scale etching of hexagonal boron nitride for device integration based on two-dimensional materials. *Nanoscale* **10**, 15205–15212 (2018).
29. Saito, A., Ayano, T. & Nomura, S. Photoresponse in h-BN/MoS_2/h-BN thin-film transistor. *Jpn. J. Appl. Phys.* **57**, 045201 (2018).
30. Khan, M. A. *et al*. Gate tunable self-biased diode based on few layered MoS_2 and WSe_2. *Chem. Mater.* **30**, 1011–1016 (2018).
31. Chao, Y. *et al*. Self-assembly of flexible free-standing 3D porous MoS_2-reduced graphene oxide structure for high-performance lithium-ion batteries. *Adv. Funct. Mater.* **27**, 1700234 (2017).
32. Leonardi, S. G. *et al*. A highly sensitive room temperature humidity sensor based on 2D-WS_2 nanosheets. *FlatChem* **9**, 21–26 (2018).
33. Kumar, K. S., Choudhary, N., Jung, Y. & Thomas, J. Recent advances in two-dimensional nanomaterials for supercapacitor electrode applications. *ACS Energy Lett.* **3**, 482–495 (2018).
34. Chang, H.-Y. *et al*. High-Performance, Highly bendable MoS_2 transistors with high-k dielectrics for flexible low-power systems. *ACS Nano* **7**, 5446–5452 (2013).
35. Manzeli, S., Allain, A., Ghadimi, A. & Kis, A. Piezoresistivity and Strain-induced Band Gap Tuning in Atomically Thin MoS_2. *Nano Lett.* **15**, 5330–5335 (2015).
36. Phuc, H. V. *et al*. Tuning the Electronic Properties, Effective mass and carrier mobility of MoS_2 monolayer by strain engineering: first-principle calculations. *J. Electron. Mater.* **47**, 730–736 (2018).
37. Wang, Y. *et al*. Strain-induced direct–indirect bandgap transition and phonon modulation in monolayer WS_2. *Nano Res.* **8**, 2562–2572 (2015).
38. Deng, S., Li, L. & Li, M. Stability of direct band gap under mechanical strains for monolayer MoS_2, $MoSe_2$, WS_2 and WSe_2. *Phys. E Low-dimensional Syst. Nanostructures* **101**, 44–49 (2018).
39. Scalise, E., Houssa, M., Pourtois, G., Afanas'ev, V. & Stesmans, A. Strain-induced semiconductor to metal transition in the two-dimensional honeycomb structure of MoS_2. *Nano Res.* **5**, 43–48 (2012).
40. Peelaers, H. & Van de Walle, C. G. Effects of strain on band structure and effective masses in MoS_2. *Phys. Rev. B* **86**, 241401 (2012).
41. Chang, C.-H., Fan, X., Lin, S.-H. & Kuo, J.-L. Orbital analysis of electronic structure and phonon dispersion in MoS_2, $MoSe_2$, WS_2. *Phys. Rev. B* **88**, 195420 (2013).
42. Lee, G.-H. *et al*. Flexible and transparent MoS_2 field-effect transistors on hexagonal boron nitride-graphene heterostructures. *ACS Nano* **7**, 7931–7936 (2013).
43. Jin, C., Lin, F., Suenaga, K. & Iijima, S. Fabrication of a freestanding boron nitride single layer and its defect assignments. *Phys. Rev. Lett.* **102**, 195505 (2009).
44. Berkdemir, A. *et al*. Identification of individual and few layers of WS_2 using Raman spectroscopy. *Sci. Rep.* **3**, 1755 (2013).
45. Li, Q. *et al*. Electric-field-induced widely tunable direct and indirect band gaps in hBN/MoS_2 van der Waals heterostructures. *J. Mater. Chem. C* **5**, 4426–4434 (2017).
46. Li, N., Su, J., Xu, Z., Li, D.-P. & Liu, Z.-T. Theoretical and experimental investigation on structural and electronic properties of Al/O/Al, O-doped WS_2. *J. Phys. Chem. Solids* **89**, 84–88 (2016).
47. Su, J., Feng, L., Pan, H., Lu, H. & Liu, Z. Modulating the electronic properties of monolayer MoS_2 through heterostructure with monolayer gray arsenic. *Mater. Des.* **96**, 257–262 (2016).
48. Rawat, A., Jena, N., Dimple, D. & De Sarkar, A. A comprehensive study on carrier mobility and artificial photosynthetic properties in group VI B transition metal dichalcogenide monolayers. *J. Mater. Chem. A* **6**, 8693–8704 (2018).
49. Feng, L., Su, J. & Liu, Z. Characteristics of lateral and hybrid heterostructures based on monolayer MoS_2: a computational study. *Phys. Chem. Chem. Phys.* **19**, 4741–4750 (2017).

50. Mak, K. F., Lee, C., Hone, J., Shan, J. & Heinz, T. F. Atomically thin MoS_2: a new direct-gap semiconductor. *Phys. Rev. Lett.* **105**, 136805 (2010).
51. Zhong, H. *et al*. Interfacial properties of monolayer and bilayer MoS_2 contacts with metals: beyond the energy band calculations. *Sci. Rep.* **6**, 21786 (2016).
52. Guan, L. & Tao, J. Mechanism of magnetic coupling in carrier-doped SnO nanosheets. *Phys. Rev. Appiedl.* **8**, 064019 (2017).
53. Shi, H., Pan, H., Zhang, Y.-W. & Yakobson, B. I. Quasiparticle band structures and optical properties of strained monolayer MoS_2 and WS_2. *Phys. Rev. B* **87**, 155304 (2013).
54. Komsa, H.-P. & Krasheninnikov, A. V. Effects of confinement and environment on the electronic structure and exciton binding energy of MoS_2 from first principles. *Phys. Rev. B* **86**, 241201 (2012).
55. Wang, L. *et al*. Slow cooling and efficient extraction of C-exciton hot carriers in MoS_2 monolayer. *Nat. Commun.* **8**, 13906 (2017).
56. Latini, S., Winther, K. T., Olsen, T. & Thygesen, K. S. Interlayer excitons and band alignment in MoS_2/hBN/WSe_2 van der Waals heterostructures. *Nano Lett.* **17**, 938–945 (2017).
57. Zhao, X. G. *et al*. Design of lead-free inorganic halide perovskites for solar cells via cation-transmutation. *J. Am. Chem. Soc.* **139**, 2630–2638 (2017).
58. Zheng, W. *et al*. Light emission properties of 2D transition metal dichalcogenides: fundamentals and applications. *Adv. Opt. Mater.* **6**, 1800420 (2018).
59. Kresse, G. & Joubert, D. From ultrasoft pseudopotentials to the projector augmented-wave method. *Phys. Rev. B* **59**, 1758–1775 (1999).
60. Kresse, G. & Furthmüller, J. Efficient iterative schemes for ab initio total-energy calculations using a plane-wave basis set. *Phys. Rev. B* **54**, 11169–11186 (1996).
61. Perdew, J. P., Burke, K. & Ernzerhof, M. Generalized gradient approximation made simple. *Phys. Rev. Lett.* **77**, 3865–3868 (1996).
62. Bardeen, J. & Shockley, W. Deformation potentials and mobilities in non-polar crystals. *Phys. Rev.* **80**, 72–80 (1950).

Acknowledgements

This work was financially supported by the National Natural Science Foundation of China (Grant 61604119, 61704131, and 61804111); Natural Science Foundation of Shaanxi Province (Grant 2017JQ6002, and 2017JQ6031); Initiative Postdocs Supporting Program (Grant BX20180234); Project funded by China Postdoctoral Science Foundation (Grant 2018M643578); Fund of the State Key Laboratory of Solidification Processing in NWPU (Grant SKLSP201857). The 111 Project (Grant B12026). The numerical calculations in this paper have been done on the HPC system of Xidian University.

Author Contributions

The idea was conceived by J.S., J.C. and J.Z. The simulation was performed by J.H. and J.Z. The data analyses were performed by J.S., Z.L., J.C. and Y.H. Tis manuscript was written by J.S., Z.L. and J.C. All authors discussed the results and contributed to the paper.

Additional Information

Supplementary information accompanies this paper at https://doi.org/10.1038/s41598-019-39970-0.

Competing Interests: The authors declare no competing interests.

Publisher's note: Springer Nature remains neutral with regard to jurisdictional claims in published maps and institutional affiliations.